

SAE Paper Number 2021-01-1188©2021 Society of Automotive Engineers International. This paper is  
Posted on this website with permission from SAE International. As a user of this website you are  
Permitted to view this paper on-line and print one copy of this paper for your use only. This paper  
may not be copied, distributed or forwarded without permission from SAE.



# The Effect of Temperature on the Molecular Compositions of External and Internal Gasoline Direct Injection Deposits

Max K. Edney and Emily F. Smith University of Nottingham

Edward Wilmot, Jacqueline Reid, and Jim Barker Innospec

Morgan R. Alexander, Colin E. Snape, and David J. Scurr University of Nottingham

**Citation:** Edney, M.K., Smith, E.F., Wilmot, E., Reid, J. et al., "The Effect of Temperature on the Molecular Compositions of External and Internal Gasoline Direct Injection Deposits," SAE Technical Paper 2021-01-1188, 2021, doi:10.4271/2021-01-1188.

## Abstract

The increased severity and prevalence of insoluble deposits formed on fuel injectors in gasoline direct injection (GDI) engines precipitates negative environmental, economic and healthcare impacts. A necessary step in mitigating deposits is to unravel the molecular compositions of these complex layered materials. But very little molecular data has been acquired. Mass spectrometry shows promise but most techniques require the use of solvents, making them unsuited for analyzing insoluble deposits. Here, we apply the high mass-resolving power and *in-situ* analysis capabilities of 3D Orbitrap™ secondary ion mass spectrometry (3D OrbiSIMS) to characterize deposits formed on the external tip and internal needle from a GDI injector. This is the first application of the technique to study internal GDI

deposits. Polycyclic aromatic hydrocarbons (PAHs) are present up to higher maximum masses in the external deposit. Lubricating oil derived sulfonates are more intense in the internal deposit, however higher mass sulfonates are only present in the external deposit. None of these molecular species have been identified in internal GDI deposits before. 3D OrbiSIMS depth profiles show that the needle deposit has a uniform deposit layer whereas the injector tip has a more complex layered structure. Comparison of 3D OrbiSIMS data suggests that the higher temperature experienced by the external injector tip explains key compositional differences and leads to growth of a thicker, more complex, layered deposit structure. The new insight into the impact that temperature has on deposit composition will aid in their mitigation and will lead to reduced vehicle emissions and cleaner air.

## Introduction

The drive for reduced emissions and more efficient vehicle operation can be partially met by clean-operating GDI based engines which are shown to give higher power output and fuel economy and reduced emissions compared to older gasoline injection strategies [1]. As such, there will be a significant number of GDI based vehicles on the road in developed nations and in developing nations where electric and hybrid vehicle technology will be slower to implement. It is predicted that in 2050, 80 % of global passenger vehicles on the road will use internal combustion based engines [2], highlighting the importance of ensuring clean operation of such engines. Approaches to reduce GDI vehicle emissions are being investigated in the industry, such as the development of gasoline particulate filters [3], adopting multiple injection strategies per cycle [4]. Or modifying fuel mixtures to improve burn characteristics and reduce emissions, especially of particulates [5]. But the formation of insoluble deposits in both external and internal GDI components threatens to counteract these strategies. Emissions of particulates are shown to be significantly affected when

deposits form [6, 7, 8, 9], thereby causing negative impacts on the environment and global human health.

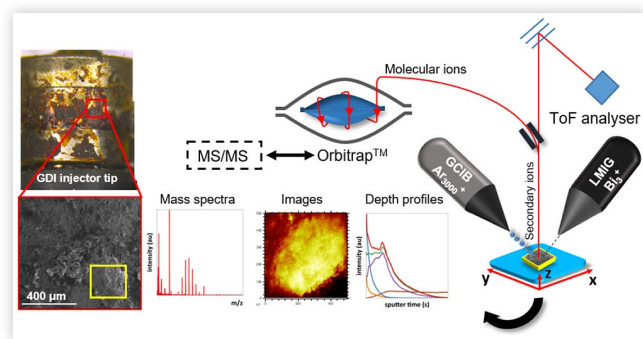
A large area of research in the field is in the development of fuel additives to ensure high efficiency and low emissions of vehicles over its lifetime. Recent work represented a paradigm-shift in the use of solubilizing additives to mitigate GDI deposits and reduce emissions, even in vehicles where deposits had previously formed [9]. However, more compositional data on GDI deposits is needed to fully understand their origin and formation mechanisms and will be vital to inform further development of fuel additives to mitigate them. This will become more important as fuel mixtures are changed in the future, such as the increased inclusion of bio-ethanol. However, deposits are complex analytes and their overall composition comprises several sources including but not limited to 'hydrocarbon' (fuel) material, and other species such as lubricating oil constituents, inorganic salts and impurities from various sources [6]. Various analysis techniques have been applied to study GDI deposits but only revealed limited information on their composition. Dearn et al. and Barker et al. used elemental analysis to discern the origin of

certain species such as from lubricating oil and uncovered trends in the elemental distribution across the injector surface [9,10]. But no molecular information on deposits was gained. The complexity, layered structure and insolubility of these deposits poses a unique analytical challenge. A recent review points out this gap in the realm of analytical instrumentation [6], and recommends that mass spectrometry techniques are best placed to give a comprehensive molecular characterization. But that an ideal technique would be able to probe sample provenance *in-situ* without the use of solvents which rules out many mass spectrometry techniques currently [6].

Time of flight secondary ion mass spectrometry (ToF-SIMS) has been demonstrated as a suitable analysis technique for *in-situ* deposit analysis, specifically on diesel deposits [11, 12, 13]. By depth profiling using a sputtering beam it can account for the deposits layered structure as well as generate chemical images to observe the distribution of ions across the samples presented surface. It was the first technique that showed deposits were layered materials and distinguished species from a range of sources such as residual lubricating oil, fuel and 'fuel contaminants' such as inorganic salts [11,14]. However, the technique uses a relatively high energy  $\text{Bi}_3^+$  analysis beam, meaning that large molecular fragments were not identified. Furthermore, the relatively low mass accuracy and mass resolving power of the ToF analyser ( $< 20,000$ ), meant that reference samples are needed to increase confidence in assignments.

A recent development in the surface analysis field was the use of the 3D OrbiSIMS technique, which combines a ToF-SIMS instrument with an Orbitrap<sup>TM</sup> mass analyser (mass resolving power  $> 240,000$ ) and a low energy argon gas cluster ion beam (GCIB) which is capable of accurately elucidating larger molecular species from the sample compared to the  $\text{Bi}_3^+$  source used in previous ToF-SIMS analysis [15]. The instrument can also perform MS/MS of identified species to confirm assignments and brings this technique in-line with other high-resolution mass spectrometry techniques [9]. A diagram of the technique is shown in Figure 1 showing its key features and modes of analysis. We also note the ability of the instrument to accommodate a variety of sample types and sizes, meaning it will be useful for analyzing new fuel injector components which are in continuous development [16].

**FIGURE 1** Schematic showing the operation modes, workflow and outputs of 3D OrbiSIMS for *in-situ* analysis of a gasoline direct injection (GDI) tip. Micrographs and data are taken from our previous work as an example [17].



We first demonstrated this technique for deposit analysis in recent work where we unveiled the spatially resolved molecular compositions of deposits on an external GDI tip, an internal diesel injector and a diesel filter component [17]. We performed depth profiles and chemical images with confirmation of assignments using MS/MS for the first time in this field and identified species up to much higher masses than in previous attempts using ToF-SIMS. This allowed us to confidently assign their origin more confidently. While it gave only elemental analysis, X-ray photoelectron spectroscopy (XPS) provided complementary quantified analysis of samples and showed them to be mainly carbonaceous, highlighting the importance of a mass spectrometry approach. But this work did not focus on samples from internal GDI components and did not compare data from the same fuel stream, which may reveal other reasons behind compositional differences aside from fuel composition.

Here, we analyze and compare datasets from an external and internal GDI injector deposit for the first time using XPS and 3D OrbiSIMS. The injector tip experiences higher temperatures than the injector needle as it is exposed to the combustion flame. We uncover key differences between deposit compositions such as the maximum size of PAH observed, the presence of inorganic salts and intensity of lubricating oil species and partly attribute compositional differences to the effect of temperature. 3D OrbiSIMS revealed species never seen before in internal GDI deposits. Depth profiling and chemical imaging of the external deposit showed similar composition to a sample analyzed by the same method in previous work [17], despite different sample provenance. While depth profiles of the internal needle deposit exhibited a uniform deposit layer above the substrate.

## Methodology

### Materials

The GDI injector used in this analysis was from a US top tier retail gasoline fuel engine test using a GM-LHU-GDI injector. The injector was retrieved and dismantled, and the injector tip and needle were then analyzed by techniques described next.

### 3D OrbiSIMS

In this work we analyzed areas of the injector tip deposit and injector needle *in-situ* using 3D OrbiSIMS. In each case different analysis areas were used to acquire each polarity datasets. An analytical repeat of positive ion data on the injector tip deposit was also acquired in a different area of the deposit.

3D OrbiSIMS analysis was conducted by using a Hybrid SIMS instrument with the technique outlined by Passarelli et al. [15]. Secondary ions were collected using the Q Exactive HF Orbitrap mass analyzer (affording a mass resolution of 240,000 at  $m/z$  200) that was calibrated using clustered silver ions prior to all sample measurements. In all profiling and imaging experiments, a 20 keV  $\text{Ar}_{3000}^+$  gas cluster ion beam

was used, defocused to 20  $\mu\text{m}$  with a duty cycle of 4.4 % and a target current of 0.23 nA, an Orbitrap™ cycle time of 200  $\mu\text{s}$  and an injection time of 500 ms was used. Charge compensation was achieved with a low-energy electron flood gun (21 eV and extraction bias of  $-20$  V) and by regulation of the main chamber with argon gas ( $9 \times 10^{-7}$  mbar) to delocalize any accumulation of charge surrounding the sample. Deposit sample data were collected over a mass range of  $m/z$  75–1125 using SurfaceLab software (version 7.1.b (IONTOF GmbH)), with the application programming interface (API) provided by Thermo Fisher for control of the Orbitrap MS portion of the instrument. Data processing was performed using SurfaceLab Version 7.1.c (ION-TOF GmbH).

Single beam depth profiles using  $\text{Ar}_{3000}^+$  ions from the gas cluster source to produce secondary ions which were analyzed by the Orbitrap analyzer (Mode 4) were acquired using one area per polarity on both samples. All analysis areas were  $300 \times 300 \mu\text{m}^2$  in size (random raster mode) and an interlaced border was used to prevent boundary effects. Profiles were acquired over a total sputter time of 22000 s (negative) and 35000 s (positive) for the injector tip deposit and 120 s (positive) 560 s (negative) for the injector needle deposit.

Chemical images were obtained from the injector tip deposit using Mode 7 of the instrument, where the gas cluster ion beam ( $\text{Ar}_{3000}^+$ ) rasters the sample surface with a low current and obtains secondary ion data at different positions. These were acquired over a total of two scans (900 s total acquisition time) with a resultant pixel size of 5  $\mu\text{m}$  and an area of  $300 \times 300 \mu\text{m}^2$  with a noninterlaced border. Images were later cropped to  $200 \times 200 \mu\text{m}^2$ , normalized to the total ion image, and scaled to match the intensity of each depth for both samples. All imaging and profiles were performed with the same settings outlined prior and with a sputtering area of  $200 \times 200 \mu\text{m}^2$ .

## X-ray Photoelectron Spectroscopy

In this work we analyzed an area on the side wall of the carbonaceous injector tip deposit and the thin film injector needle deposit. We performed argon gas cluster ion beam etching of both deposits, we present the XPS data after cleaning of the injector tip deposits surface to remove contaminants and adventitious carbon using the beam. Analytical data for the injector needle deposit was taken from the very top surface (0 s etch) to avoid inclusion of the metal substrate peaks.

Samples were mounted on a standard Kratos sample bar (13 cm  $\times$  1.5 cm) using double-sided adhesive non-conducting tape. Samples were then subjected to XPS analysis using the Kratos AXIS ULTRA DLD liquid phase photoelectron spectrometer (LiPPS) with a monochromated Al  $K\alpha$  X-ray source (1486.6 eV) with a source power of 120 W. Gas cluster ion beam etching (20 keV  $\text{Ar}_{500}^+$  cluster beam) over etch area of 0.75  $\text{mm}^2$  on the injector tip deposit was performed prior to analysis for a total etch time of 120 s (120 s etch time). This was not performed on the injector needle deposit. The XPS spectrum for both samples were then acquired with photoelectrons collected using the electrostatic lens mode with a

circular aperture of 110  $\mu\text{m}$ . We used the optical camera to ensure the analysis area was central in the etched crater of the etched injector tip deposit. Spectra were acquired with the Kratos VISION II software. Low-resolution survey spectra of both samples were recorded between a binding energy ranges 1200 to  $-5$  eV, a charge neutralizer filament was used to prevent surface charging; the pass energy was 160 eV, both with a step energy of 1 eV. The spectra were charge corrected to the surface C 1s peak (adventitious carbon) set to 285 eV and used to estimate the total atomic % of the detected elements using CasaXPS (version 2.3.22 PR1.0) software. Peak positions were referenced to the XPS reference pages of XPSFitting [18].

## Scanning Electron Microscopy

SEM micrographs were acquired for all samples using a FEI Quanta 650 ESEM instrument. All sample analysis was performed in low vacuum (60 Pa) to prevent sample charging, with an incident energy of 20 kV.

## Optical Microscopy

Optical microscopy images of the gasoline and diesel injector deposit samples were taken with a Leica M205 FA Stereo light microscope.

## Miscellaneous

Depth profiles presented in Figure 6 were plotted using Veusz (Version 3.2.1, Jeremy Sanders). Chemical structures were drawn using ChemDraw (version 18.2)

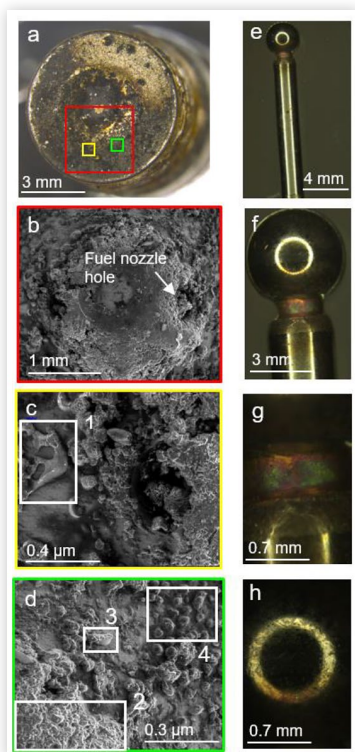
## Results and Discussion

### Visual and Elemental Analysis of Deposits

To obtain a visual understanding of the injector deposits we performed optical microscopy on the external injector tip and internal needle, and performed scanning electron microscopy (SEM) on the injector tip (including the nozzle and the side wall of the tip), data is displayed in Figure 2.

There is clearly a significant build-up of deposit on the external part of the injector including the injector sidewall (Figure 1), including the injector nozzle (Figure 2a), and the fuel nozzle hole itself (Figure 2b), it is apparent that this blockage will severely impact fuel spray and thus emissions. Significant blockage can also lead to injector failure as well. Of note is the range of deposit morphologies present on the injector tip, highlighted by the numbered white boxes in Figure 2c–d. Namely a visibly thin film of deposit (1 in Figure 2c), likely originating from residual droplets of fuel which have leaked from the injector nozzle. Next, small spherical particles of deposits which have been observed by other works using this technique on GDI deposits (4 in Figure 2d) [9].

**FIGURE 2** a, Optical micrographs of a GDI external tip deposit. b-d, scanning electron micrographs of injector deposits on the tip nozzle showing different morphologies highlighted by the numbered white boxes. e-h, optical micrographs of an internal injector needle.



Finally, a visibly thicker deposit type which has been observed before and is attributed to a predominately carbonaceous morphology (2 and 3 in Figure 2d). There was less variation in deposit morphology on the side-wall deposit of the tip, which exhibited a thick carbonaceous deposit structure (Figure 1). It is likely that the absence of fuel droplets on this part of the component results in a more homogenous deposit morphology. Owing to the increased size of these deposits this will be targeted by 3D OrbiSIMS in this work. By contrast, the injector needle showed a marked different morphology, illustrating a thin film structure with more discoloration closer to the injector ball (Figure 2e-h). Interrogation of different areas shows a similar ‘deposit film’ morphology. There are signs of small ‘scratches’ on the injector ball (Figure 2h) which may act as nucleation points for carbonaceous deposit formation. Abdallah et al. demonstrated that a visibly thin film deposit of this type can still contain a significant level of deposition, however [19].

Quantified elemental information on the deposits were then obtained using X-ray photoelectron spectroscopy, we analyzed the injector tip deposit after etching for 120 s to remove surface contamination. We analyzed the very top surface of the injector needle (0 s etch time) to avoid inclusion of the metal substrate peaks on this thin film deposit, XPS spectra is shown in Figure 3 and data is tabulated in Table 1.

XPS spectra of both samples appeared similar aside from the lack of an intense signal from the substrate (Fe 2p and

**FIGURE 3** X-ray photoelectron spectroscopy analysis of injector tip and needle deposits. Spectra of both samples with key assignments displayed. Data from the injector tip deposit was taken after cleaning with the Ar<sub>500</sub><sup>+</sup> beam, data from the injector needle is taken from the top surface of the deposit.

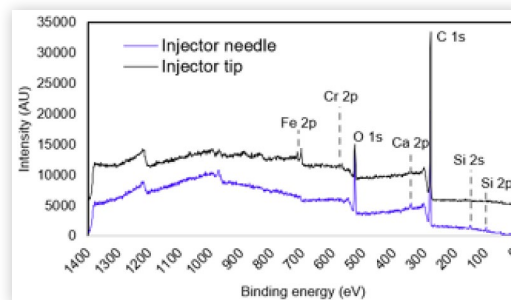


**TABLE 1** Summarized elemental compositions calculated from peak area of XPS analysis shown in Figure 3.

Atomic concentration (at. %)		
Peak	External tip deposit	Internal needle deposit
C 1s	87.2	79.1
O 1s	8	17.3
Fe 2p	2.1	0
Cr 2p	1.3	0
Ca 2p	0.6	0.92
S 2s	0.4	0
Si 2p	0.5	2.7

Cr 2p) in the needle sample (Figure 3). We note a very minor signal for Fe on the blue spectra for the internal needle despite taking this data after etching for 0 s, suggesting a very thin layer of deposit has formed on this component. Interrogation of the wide-scan XPS data highlights that both deposits are predominately carbonaceous (up to 87 % C in the injector tip) with differences being explained by minor contributors (Table 1). There is a slightly increased contribution of Ca in the injector needle which may suggest higher levels of lubricating oil contamination in this component. Si was ubiquitous and is attributed to silicone contamination of the samples. S was only found in the injector tip, but its low contribution (0.3 %) means that it may be present in the needle but below the minimum sensitivity of the instrument and care should be taken reading its exact value. Oxygen was higher in the needle and has several possible origins such as fuel derived species (alcohols or ethers) or from the injector substrate (metal oxides). Fe and Cr were only in the injector tip (up to 2 %) and is attributed to areas of exposed clean metal substrate which were analyzed, the rough ‘patchy’ topography of the deposit is shown in the micrograph in Figure 1. These peaks were not present in the injector needle deposit as we did not etch this sample, suggesting the needle deposit has smoother topography and a thinner layer than the tip deposit. Overall, both deposits are predominantly carbonaceous despite their differing morphology, with trace contributions of lubricating oil constituents.

Other elements such as N have been detected in GDI deposits using XPS, in this work we also found Fe and Cr substrate originating from substrate despite not performing sample etching [17], and results should be considered as a collective across different works. While elemental analysis is useful as an initial probing of deposit chemistry it is evidently limited in its ability for a comprehensive chemical characterization.

## Identifying Molecular Species with 3D OrbiSIMS

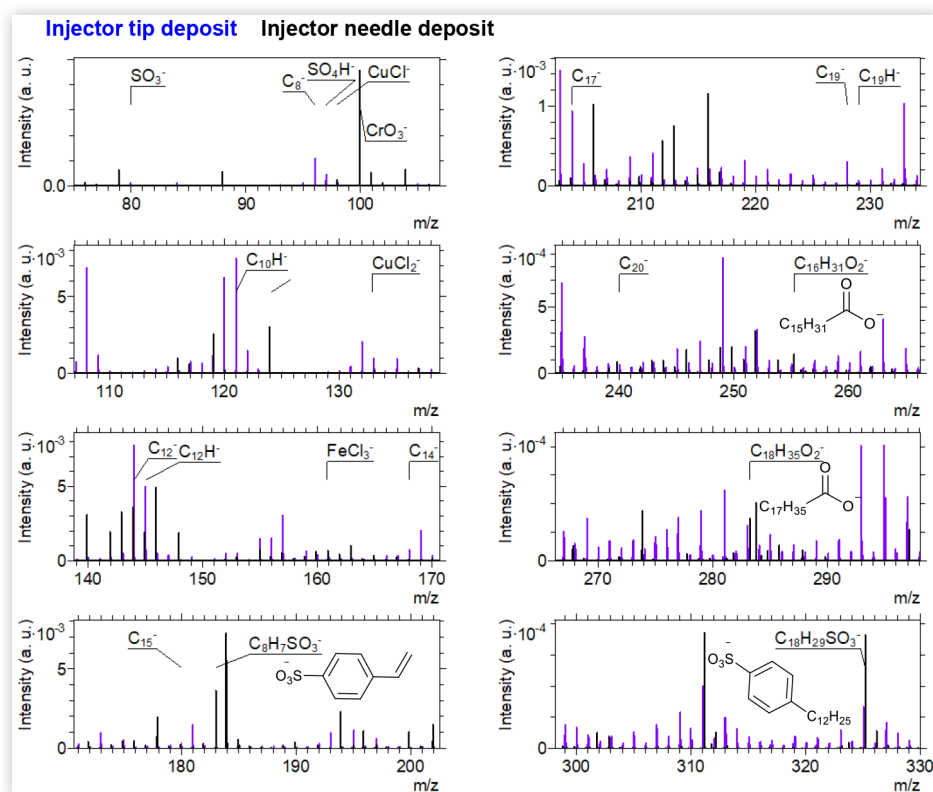
Negative ion spectra for the external injector tip and internal injector needle deposit are displayed in Figure 4 in the mass range of  $m/z$  75-330 with key assignments labelled.

By overlaying normalized ion spectra and comparing intensities of common species (highlighted by the color of each peak in Figure 4 showing which component had the highest intensity of each ion), we identified key differences between injector tip and needle deposit chemistries for the first time (ion data for can be found in the appendix). Alkyl benzyl sulfonate ions ( $[C_6H_4SO_3(C_nH_{(2n+1)})]^-$ , termed sulfonates from here on) were accurately identified in both deposits, including the cited molecule added to additive packages,  $C_{18}H_{29}SO_3^-$  [20,21]. Sulfonates were more intense in the injector needle, shown by the prominence of the black spectral

lines in Figure 4 ( $C_8H_7SO_3^-$  and  $C_{18}H_{29}SO_3^-$ ). What is of note is that sulfonate ions of higher masses (such as  $C_{30}H_{53}SO_3^-$ ) were present in the injector tip and not in the injector needle. We calculated the mass difference of different sulfonate fragments and propose the high mass species arise from alkyl extension reactions of the deposited sulfonate residue with fuel derived species. For example,  $C_{26}H_{45}SO_3^-$  can be explained by addition between sulfonate and different numbers of an octane molecule ( $C_{26}H_{45}SO_3^- = C_{18}H_{29}SO_3^- + C_8H_{16}$ ), once the negative charge and proton abstraction has been accounted for. In our previous work we also found these high mass ions such as  $C_{42}H_{77}SO_3^-$  in GDI tip deposits and confirmed their assignment with MS/MS [17]. The fact that these ions are not present in the needle deposit suggests this reactivity does not occur in this component and we attribute this to the reduced temperature this component experiences compared to the external injector tip deposit.

Linear carboxylic acids such as stearic and palmitic acid were identified in both components and were most intense in the needle deposit (Figure 4). These likely derive from the lubricating oil since the base oils can contain  $C_8$ - $C_{22}$  linear monocarboxylic acids [22], however, they have also been ascribed as being derived from corrosion inhibitor additive packages in the past [23]. The lack of Na in the deposit shown by XPS suggests these are not derived from sodium carboxylate salts. XPS also shows that S was present in very low concentrations (Figure 3), suggesting a trace amount of

**FIGURE 4** Negative ion 3D OrbiSIMS depth profile accumulation spectra, normalized to the total ion count, in the range of  $m/z$  75 - 360. Spectra from the two samples are overlaid, blue = injector tip deposit and black = injector needle deposit. Putative chemical structures of some species are displayed. We assign key species on the spectra with < 2 ppm mass deviation. Ion data can be found in the appendix.



lubricating oil constituents (sulfonates) despite their high intensity in the 3D OrbiSIMS spectra. This highlights the need for complementary analysis techniques such as XPS to overcome preferential ionization of species in SIMS analysis and to aid in assigning the origin of species.

The injector needle also contained ions corresponding to the metal substrate such as  $\text{CrO}_3^-$ , this ion was far less intense in the injector tip (appendix), we propose the rough ‘patchy’ topography of the injector tip deposit means that some exposed areas of metal were analyzed in this sample, correlating with XPS (Table 1). Inorganic salts such as sodium chloride ( $\text{NaCl}$ ), copper chloride ( $\text{CuCl}$ ) and iron chloride ( $\text{FeCl}_3^-$ ) were identified and were most intense in the injector needle (Figure 4).

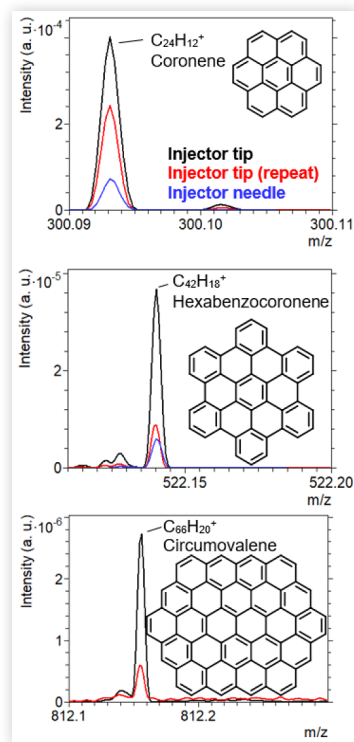
Overall, the negatively ionizing species were mostly common to both sample types, the injector needle appears to have a higher contribution from lubricating oil species and inorganic salts. It is likely that the combustion flame, which only the injector tip was exposed to, promotes further degradation of lubricating oil species.

## Carbonaceous Species

Unsaturated carbonaceous negative ions ( $\text{C}_n^-$  and  $\text{C}_n\text{H}^-$ ) were identified in both samples and were more intense in the injector tip deposit and present up to higher maximum masses compared with the injector needle sample (Figure 4 and appendix). Their origin is most likely residual fuel, but from spectral analysis alone it is difficult to confirm. SIMS analysis has shown these to be sourced from graphitic like materials [24], suggesting it marks ordered carbonaceous material in the deposit. Conversely, positive ion data showed intact molecules (positive radicals) corresponding to PAHs in both samples, work has yet to show PAHs in GDI needle deposits. PAHs are noted as being particularly difficult to identify by *in-situ* analysis which showcases the strength of 3D OrbiSIMS for detecting large intact species. Ion data for three example PAHs from both samples, including an analytical repeat dataset from a different area on the injector tip deposit are displayed in Figure 5.

PAH intensity and speciation showed insightful differences between sample compositions on both component deposits. Coronene (above), hexabenzocoronene (middle) and circumvalene (below) were accurately assigned with a mass error < 2 ppm in all samples and repeat areas (Figure 5). It should be noted that isomeric structures are possible, for example, with structures containing 5-membered rings and it is unfeasible to distinguish the specific structure from accurate mass alone. We identified PAHs in the needle deposit up to  $m/z$  522 (hexabenzocoronene), which was a lower maximum mass compared to the injector tip deposit, shown in the absence of a signal in blue for circumvalene (Figure 5). However, it is still notable that large PAHs were present in an internal GDI deposit, despite its lack of carbonaceous morphologies compared to the injector tip (Figure 2), particularly since the high pressure the needle experiences is expected to suppress carbonaceous deposit formation. We attribute the difference in maximum mass of PAH between components to the lower temperature that the injector needle experiences.

**FIGURE 5** 3D OrbiSIMS positive ion spectra in selected mass regions showing speciation of high mass aromatics for the injector tip deposit (black), a repeat of this sample in a separate area (red) and the injector needle (blue). Putative chemical structures are also displayed, other isomeric structures are possible from the assigned formula.



The temperature effect also explains the speciation of higher maximum mass negative carbonaceous ions in the injector tip ( $\text{C}_{20}^-$ ) compared with the injector needle ( $\text{C}_{12}^-$ ) (see appendix). It has been hypothesized that PAHs originate from temperature induced aromatization of gasoline in the engine [17]. Evidently the extent of carbonaceous deposit formation and comparisons between component deposit type can be partially explained by the effect of temperature and highlights how deposit composition is explained by both the deposition of species and their subsequent reactivity.

## Combining 3D OrbiSIMS Depth Profiling and Chemical Imaging

We next performed depth profiles on both the injector needle and tip deposit to understand differences in their layered structure, we also performed chemical imaging of the external injector tip deposit at both the surface and a lower depth after reaching an interface of the deposit. Data from both samples are displayed in Figure 6.

Evidently the injector tip and needle deposit have a marked different layering structure, in this case the tip deposit (Figure 6a) showed distinct layers, whereas the organic layer of the injector needle deposit (above the  $\text{CrO}_3^-$  substrate) exhibited a uniform distribution of species above the substrate

**FIGURE 6** Combining 3D OrbiSIMS  $\text{Ar}_{3000}^+$  depth profiling and chemical imaging on a GDI tip deposit. a, left, depth profiles of the injector tip deposit with the lower imaging position marked by the line on the profile. Right, chemical images ( $200 \mu\text{m}^2$ ) of selected ions at the surface and interface of the injector tip deposit. b, depth profiles of the injector needle deposit.

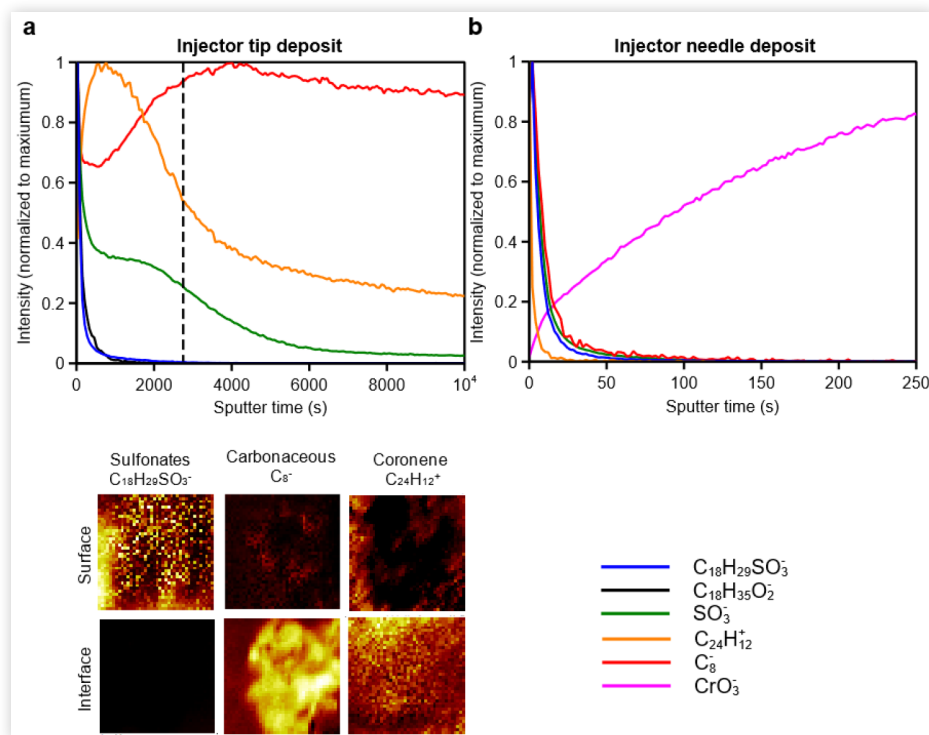


(Figure 6b). It is likely that the lack of high mass PAHs limits its growth into a layered deposit structure, suggesting they are key constituents of the carbonaceous matrix. The injector tip depth profile shows that the upper layer consists of sulfonates ( $\text{C}_{18}\text{H}_{29}\text{SO}_3^-$ ) and carboxylic acids ( $\text{C}_{18}\text{H}_{35}\text{O}_2^-$ ), (Figure 6a). It is likely that the sulfonates and carboxylic acids break down readily once deposited, partially *via* loss of alkyl chain and so are not embedded in lower deposit layers. Therefore, only smaller organic fragments exist in lower depths for species which are trace contaminants. The profile of the sulfonate head group,  $\text{SO}_3^-$ , exemplifies this point since it is present not just at the surface. Coronene was present at most layers of the injector tip deposit but was most prevalent in the middle portion (Figure 6a) and the lowest deposit layer of this sample was marked with the carbonaceous ions ( $\text{C}_8^-$ ), which corroborates with data from previous work on another GDI injector tip deposit [17].

Imaging of the surface and lower deposit depth of the external tip deposit shows informative contrast of species (Figure 6a). The sulfonate ion is evidently surface localised and has a relatively non-uniform distribution, which allies with our hypothesis that these are molecules that are embedded in the deposit matrix from lubricating oil contamination. The previous issue of identifying the origin of carbonaceous ions in this sample is overcome by chemical imaging, since ions had a localised clustering and were more intense at the lower deposit depth, suggesting their origin is from the breakdown of fuel species over time and not lubricating oil contamination. The increased carbonaceous content correlates with previous work where we attributed these species as

originating from condensed aromatic clusters [17]. The overall agreement of the combined depth profile and imaging data between this sample and the GDI tip analyzed in our original work is of note, since the samples have different provenance. This points to a universally common composition of the GDI deposits matrix and will be explored in future work.

## Conclusions

In this work we have used 3D OrbiSIMS and XPS to provide a quantified molecular characterization of deposits formed on external and internal GDI components and compared sample datasets for the first time. 3D OrbiSIMS revealed molecular species not seen in internal GDI deposits before. Comparison of data between both systems highlighted several key points:

- Despite differing morphologies, the external tip and internal needle deposits consisted mainly of carbonaceous species.
- Lubricating oil derived alkyl benzyl sulfonates were common to both samples, but those of higher mass were found only in the external injector tip deposit.
- Carbonaceous ions and PAHs were present in higher intensity and up to higher maximum masses in the external tip deposit.
- Depth profiling showed markedly different deposit layering, with only a thin layer structure in the needle

deposit. We attribute this to the differing distribution of high mass aromatics, such as PAHs.

- These key compositional differences can be partially explained by the effect of higher temperature experienced by the external injector tip from the combustion chamber.

Overall, the combination of XPS and 3D OrbiSIMS is a new approach to characterize deposits, and new insight from these techniques into their composition and the influence of temperature across different engine components will provide industry with vital information to mitigate them. This will aid longer term efforts to reduce vehicle emissions and improve global air quality.

## References

- Zhao, F., Lai, M.-C., and Harrington, D., "Automotive Spark-Ignited Direct-Injection Gasoline Engines," *Prog. Energy Combust. Sci.* 25, no. 5 (1999): 437-562, doi:10.1016/s0360-1285(99)00004-0.
- Bloomberg New Energy Finance, "Electric Vehicle Outlook," 2019.
- Boger, T., Glasson, T., Rose, D., Ingram-Ogunwumi, R. et al., "Next Generation Gasoline Particulate Filters for Uncatalyzed Applications and Lowest Particulate Emissions," SAE Technical Paper 2021-01-0584 (2021). <https://doi.org/10.4271/2021-01-0584>.
- Whitaker, P., Kapus, P., Ogris, M., and Hollerer, P., "Measures to Reduce Particulate Emissions from Gasoline DI engines," *SAE Int. J. Engines* 4, no. 1 (2011): 1498-1512. <https://doi.org/10.4271/2011-01-1219>.
- Yang, J., Roth, P., Durbin, T.D., Shafer, M.M. et al., "Emissions from a Flex Fuel GDI Vehicle Operating on Ethanol Fuels Show Marked Contrasts in Chemical, Physical and Toxicological Characteristics as a Function of Ethanol Content," *Sci. Total Environ.* 683 (2019): 749-761. <https://doi.org/10.1016/j.scitotenv.2019.05.279>.
- Edney, M.K., Barker, J., Reid, J., Scurr, D.J. et al., "Recent Advances in the Analysis of GDI and Diesel Fuel Injector Deposits," *Fuel* 272 (2020): 117682, doi:10.1016/j.fuel.2020.117682.
- Ding, H., Zhang, W., Ma, X., Shuai, S. et al., "The Impact of GDI Injector Deposits on Engine Combustion and Emission," SAE Technical Paper 2017-01-2248 (2017). <https://doi.org/10.4271/2017-01-2248>.
- Jiang, C., Xu, H., Srivastava, D., Ma, X. et al., "Effect of Fuel Injector Deposit on Spray Characteristics, Gaseous Emissions and Particulate Matter in a Gasoline Direct Injection Engine," *Appl. Energy* 203 (2017): 390-402, doi:10.1016/j.apenergy.2017.06.020.
- Reid, J., Mulqueen, S., Langley, G., Wilmot, E. et al., "The Investigation of the Structure and Origins of Gasoline Direct Injection (GDI) Deposits," SAE Technical Paper 2019-01-2356 (2019). <https://doi.org/10.4271/2019-01-2356>.
- Dearn, K., Xu, J., Ding, H., Xu, H. et al., "An Investigation into the Characteristics of DISI Injector Deposits Using Advanced Analytical Methods," *SAE Int. J. Fuels Lubr.* 7, no. 3 (2014): 771-782. <https://doi.org/10.4271/2014-01-2722>.
- Barker, J., Snape, C., and Scurr, D., "Information on the Aromatic Structure of Internal Diesel Injector Deposits From Time of Flight Secondary Ion Mass Spectrometry (ToF-SIMS)," SAE Technical Paper 2014-01-1387 (2014). <https://doi.org/10.4271/2014-01-1387>.
- Dallanegra, R. and Caprotti, R., "Chemical Composition of Ashless Polymeric Internal Diesel Injector Deposits," SAE Technical Paper 2014-01-2728 (2014). <https://doi.org/10.4271/2014-01-2728>.
- Feld, H. and Oberender, N., "Characterization of Damaging Biodiesel Deposits and Biodiesel Samples by Infrared Spectroscopy (ATR-FTIR) and Mass Spectrometry (TOF-SIMS)," *SAE Int. J. Fuels Lubr.* 9, no. 3 (2016): 717-724. <https://doi.org/10.4271/2016-01-9078>.
- Barker, J., Snape, C., and Scurr, D., "A Novel Technique for Investigating the Characteristics and History of Deposits Formed Within High Pressure Fuel Injection Equipment," *SAE Int. J. Fuels Lubr.* 5, no. 3 (2012): 1155-1164. <https://doi.org/10.4271/2012-01-1685>.
- Passarelli, M.K., Pirkl, A., Moellers, R., Grinfeld, D. et al., "The 3D OrbiSIMS—Label-Free Metabolic Imaging with Subcellular Lateral Resolution and High Mass-Resolving Power," *Nat. Methods* 14 (2017): 1175.
- Beatrice, C., Belgiorno, G., Di Blasio, G., Mancaruso, E. et al., "Analysis of a Prototype High-Pressure "Hollow Cone Spray" Diesel Injector Performance in Optical and Metal Research Engines," SAE Technical Paper 2017-24-0073 (2017). <https://doi.org/10.4271/2017-24-0073>.
- Edney, M.K., Lamb, J.S., Spanu, M., Smith, E.F. et al., "Spatially Resolved Molecular Compositions of Insoluble Multilayer Deposits Responsible for Increased Pollution from Internal Combustion Engines," *ACS Appl. Mater. Interfaces* 12, no. 45 (2020): 51026-51035, doi:10.1021/acsaami.0c14532.
- XPS fitting, "XPS reference pages," [www.XPSFitting.com](http://www.XPSFitting.com), Apr. 2021.
- Abdallah, D.J., Berkhou, S.K., Wrigley, K.B., Watkins, M.I. et al., "Demistifying the Impact Diesel Fuel Bulk Composition PLays in Internal Injector Deposits with VASEtle," in *International Symposium on Stability, Handling and use of Liquid Fuels*, 2017.
- Nassar, A.M., Ahmed, N.S., El-shazly, R.I., and Abd el Menem, Y.K., "Preparation and Evaluation of the Mixtures of Sulfonate and Phenate as Lube Oil Additives," *Int. J. Ind. Chem.* 8, no. 4 (2017): 383-395, doi:10.1007/s40090-017-0128-x.
- Geng, Y., Huang, J., Tan, B., Xu, Y. et al., "Efficient Synthesis of Dodecylbenzene Sulfonic Acid in Microreaction Systems," *Chem. Eng. Process. - Process Intensif.* 149 (2020): 107858. <https://doi.org/10.1016/j.cep.2020.107858>.
- Rudnick, L.R., *Synthetics, Mineral Oils, and Bio-Based Lubricants*, 3rd ed. (Boca Raton: CRC Press, 2020), doi:10.1201/9781315158150, ISBN:9781315158150
- Technical Committee of Petroleum Additive Manufacturers in Europe, "Fuel Additives: Uses and Benefits," [https://www.atc-europe.org/public/Doc113\\_2013-11-20.pdf](https://www.atc-europe.org/public/Doc113_2013-11-20.pdf), 2013.

24. Xie, W., Weng, L.-T., Ng, K.M., Chan, C.K. et al., "Defects of Clean Graphene and Sputtered Graphite Surfaces Characterized by Time-of-Flight Secondary Ion Mass Spectrometry and X-ray Photoelectron Spectroscopy," *Carbon N. Y.* 112 (2017): 192-200. <https://doi.org/10.1016/j.carbon.2016.11.002>.

## Contact Information

### Jim Barker Dr.

Innospec Limited Innospec Manufacturing Park  
Oil Sites Road, Ellesmere Port Cheshire, CH65 4EY England  
+44 151 355 3611

[Jim.Barker@innospecinc.com](mailto:Jim.Barker@innospecinc.com)

<http://www.innospecinc.com>

## Acknowledgments

We thank David Knight (Innospec Ltd.) for breaking open injector samples prior to analysis. This research is funded and

supported by the Engineering and Physical Sciences Research Council (EPSRC) and Innospec Ltd. The project is part of the Centre for Doctoral Training in Carbon Capture and Storage and Cleaner Fossil Energy (EPSRC grant EP/L016362/1). The EPSRC is gratefully acknowledged for the following grants: "3D OrbiSIMS: Label free chemical imaging of materials, cells and tissues" funding that supported this work (grant EP/P029868/1); and the EPSRC grant for the Kratos LiPPS XPS instrument, EP/K005138/1.

## Definitions/Abbreviations

**3D OrbiSIMS** - 3D Orbitrap™ secondary ion mass spectrometry

**GDI** - Gasoline direct injection

**PAH** - Polycyclic aromatic hydrocarbon

**SEM** - Scanning electron microscopy

**XPS** - X-ray photoelectron spectroscopy

## Appendix

**TABLE A1** Negative ion data table of key species identified using 3D OrbiSIMS. Data is from, a) Injector tip deposit, b) Injector needle deposit, and was exported from Surface Lab 7. Mass deviation refers to the mass difference between the ions observed and expected mass in ppm (parts per million). AU, arbitrary units.

Injector tip deposit			
Center Mass (u)	Assignment	Mass deviation (ppm)	Peak area (AU)
79.957067	SO <sub>3</sub> <sup>-</sup>	-3.70744	294407274.5
92.927895	NaCl <sub>2</sub> <sup>-</sup>	-1.385249	66728.22
96.000394	C <sub>8</sub> <sup>-</sup>	-1.612967	2476056959
96.959992	SO <sub>4</sub> H <sup>-</sup>	-1.145556	483097791.8
N/A	CuCl <sup>-</sup>	NOT PRESENT	
99.925747	CrO <sub>3</sub> <sup>-</sup>	-0.576939	2089209.86
121.008291	C <sub>10</sub> H <sup>-</sup>	-0.685133	843439669.5
144.000407	C <sub>12</sub> <sup>-</sup>	-0.982304	885052473
145.008256	C <sub>12</sub> H <sup>-</sup>	-0.808359	577501322.2
160.841935	FeCl <sub>3</sub> <sup>-</sup>	-0.707965	10637.47
168.000412	C <sub>14</sub> <sup>-</sup>	-0.812636	94337288.81
180.000455	C <sub>15</sub> <sup>-</sup>	-0.518602	39054629.71
183.012084	C <sub>8</sub> H <sub>7</sub> SO <sub>3</sub> <sup>-</sup>	-0.298697	71499254.56
204.000385	C <sub>17</sub> <sup>-</sup>	-0.802696	110276467.3
228.000498	C <sub>19</sub> <sup>-</sup>	-0.223328	36870452.13
229.00838	C <sub>19</sub> H <sup>-</sup>	0.028317	8179214.59
240.000532	C <sub>20</sub> <sup>-</sup>	-0.068567	7692389.01
255.233092	C <sub>16</sub> H <sub>31</sub> O <sub>2</sub> <sup>-</sup>	0.539951	1829649.95
283.264347	C <sub>18</sub> H <sub>35</sub> O <sub>2</sub> <sup>-</sup>	0.32756	1886796.86
325.184309	C <sub>18</sub> H <sub>29</sub> SO <sub>3</sub> <sup>-</sup>	0.062801	10578874.62
339.199883	C <sub>19</sub> H <sub>31</sub> SO <sub>3</sub> <sup>-</sup>	-0.166396	5372771.93
437.309584	C <sub>26</sub> H <sub>45</sub> SO <sub>3</sub> <sup>-</sup>	0.21577	249441.27
465.340824	C <sub>28</sub> H <sub>49</sub> SO <sub>3</sub> <sup>-</sup>	0.074424	101220.68
479.356579	C <sub>29</sub> H <sub>51</sub> SO <sub>3</sub> <sup>-</sup>	0.291454	169514.26
493.372288	C <sub>30</sub> H <sub>53</sub> SO <sub>3</sub> <sup>-</sup>	0.402009	16345.87

b)

Injector needle deposit			
Center Mass (u)	Assignment	Mass deviation (ppm)	Peak area (AU)
79.957104	SO <sub>3</sub> <sup>-</sup>	-3.246292	31361141.32
92.927893	NaCl <sub>2</sub> <sup>-</sup>	-1.406125	140498.31
96.000477	C <sub>8</sub> <sup>-</sup>	-0.740976	1162911.56
96.960053	SO <sub>4</sub> H <sup>-</sup>	-0.513407	3766461.23
97.899022	CuCl <sup>-</sup>	0.199886	25343.33
99.925665	CrO <sub>3</sub> <sup>-</sup>	-1.39163	2374376623
121.008293	C <sub>10</sub> H <sup>-</sup>	-0.668607	412165.41
132.867787	CuCl <sub>2</sub> <sup>-</sup>	-0.510081	260866.57
144.000476	C <sub>12</sub> <sup>-</sup>	-0.503583	58429.13
145.008337	C <sub>12</sub> H <sup>-</sup>	-0.254088	95968.46
160.842315	FeCl <sub>3</sub> <sup>-</sup>	1.655659	2077.16
N/A	C <sub>14</sub> <sup>-</sup>	NOT PRESENT	
N/A	C <sub>15</sub> <sup>-</sup>	NOT PRESENT	
183.012119	C <sub>8</sub> H <sub>7</sub> SO <sub>3</sub> <sup>-</sup>	-0.106631	93708441.86
N/A	C <sub>19</sub> <sup>-</sup>	NOT PRESENT	
N/A	C <sub>19</sub> H <sup>-</sup>	NOT PRESENT	
N/A	C <sub>20</sub> <sup>-</sup>	NOT PRESENT	
255.233253	C <sub>16</sub> H <sub>31</sub> O <sub>2</sub> <sup>-</sup>	1.170473	3880297.95
283.264506	C <sub>18</sub> H <sub>3</sub> SO <sub>2</sub> <sup>-</sup>	0.889484	3987266.41
325.184524	C <sub>18</sub> H <sub>29</sub> SO <sub>3</sub> <sup>-</sup>	0.721666	10024047.42
339.200094	C <sub>19</sub> H <sub>31</sub> SO <sub>3</sub> <sup>-</sup>	0.455633	6884376.54
N/A	C <sub>26</sub> H <sub>45</sub> SO <sub>3</sub> <sup>-</sup>	NOT PRESENT	
N/A	C <sub>28</sub> H <sub>49</sub> SO <sub>3</sub> <sup>-</sup>	NOT PRESENT	
N/A	C <sub>29</sub> H <sub>51</sub> SO <sub>3</sub> <sup>-</sup>	NOT PRESENT	
N/A	C <sub>30</sub> H <sub>53</sub> SO <sub>3</sub> <sup>-</sup>	NOT PRESENT	